

1
2
3
4
5
6
7
8
9
10
11
12
13
14
15
16
17
18
19
20
21
22
23
24
25
26
27
28

Revision 1

Solid solution of CaSiO_3 and MgSiO_3 perovskites in the lower mantle: The role of ferrous iron

Feiwu Zhang^{1*}, Tingting Xiao^{1,2}, Joshua M. R. Muir^{1†}

¹ State Key Laboratory of Ore Deposit Geochemistry, Institute of Geochemistry, Chinese Academy of Sciences, Guiyang, 550081, China

² CAS Key Laboratory of Crust-Mantle Materials and Environments, School of Earth and Space Sciences, University of Science and Technology of China, Hefei 230026, China

* zhangfeiwu@mail.gyig.ac.cn

† j.m.r.muir@mail.gyig.ac.cn

Abstract

The solid solution between CaSiO_3 and MgSiO_3 perovskites is an important control on the properties of the lower mantle but the effect of one of the most important impurity elements (iron) on this solution is largely unknown. Using density functional theory (DFT), ferrous iron's influence on the reciprocal solubility of MgSiO_3 and CaSiO_3 perovskite (forming a single Ca-Mg mixed perovskite phase) was calculated under pressures and temperatures of 25 - 125 GPa and 0 - 3000 K, respectively. Except at iron-rich conditions, ferrous iron preferentially partitions into the mixed perovskite phase over bridgmanite. This is a small effect (partitioning coefficient $K_D \sim 0.25 - 1$), however, when compared to the partitioning of ferrous iron to ferropericlase which rules out perovskite phase mixing as a mechanism for creating iron-rich regions in the mantle. Iron increases the miscibility of Ca and Mg perovskite phases and reduces the temperature at which the two perovskite phases mix but this effect is highly nonlinear. We find that for a pyrolytic mantle ($\text{Ca}\% = 12.5$ where $\text{Ca}\% = \text{Ca} / (\text{Ca} + \text{Mg})$) a perovskite ferrous iron concentration of $\sim 13\%$ leads to the lowest mixing temperature and the highest miscibility. With this composition, 1% ferrous iron in a pyrolytic composition would lead to mixing at

29 ~120 GPa along the geothermal gradient, and 6.25% ferrous iron leads to mixing at ~115 GPa and 13%
30 ~110 GPa. At high iron concentrations, Fe starts to impair miscibility, with 25% ferrous iron leading to
31 mixing at ~120 GPa. Thus, in normal pyrolytic mantle, iron could induce a small amount of Ca-pv and
32 Mg-pv mixing near the D" layer but it generally partitions to ferropericlase instead and does not impact
33 mixing. Extremely iron rich parts of the lower mantle such as ULVZs or the CMB (potentially) are also
34 not a likely source of phase mixed perovskites due to the nonlinear effect of ferrous iron on phase
35 mixing.

36

37 **Keywords**

38 CaSiO₃, MgSiO₃, Iron, miscibility, the lower mantle

39 **Introduction**

40 Earth's lower mantle, extending from 660 to 2890 km in depth, occupies nearly 75% of the mass of the
41 bulk silicate Earth. Assuming that the lower mantle is pyrolytic and isochemically similar to the upper
42 mantle, MgSiO₃ perovskite (Bridgmanite) is considered to be the most abundant phase in the lower mantle,
43 accounting for about 70% of the lower mantle, followed by ferropericlase (about 20%), and finally the least
44 abundant phase is CaSiO₃-rich perovskite (Davemaoite) accounting for around 6-12% (Anderson et al. 1989;
45 O'Neill and Jeanloz 1990). Mg-rich silicate perovskite (Mg-pv) and CaSiO₃-rich perovskite (Ca-pv) are thus
46 two of the main components of the lower mantle and subducted plates. Due to their similarity in chemical
47 formula and structure, these two phases can dissolve into each other to some extent, forming a single
48 Mg_{1-x}Ca_xSiO₃ phase. Mixing of these phases is potentially important as a chemically mixed Ca-Mg-pv
49 phase will likely behave differently to a physical mixture of Ca-pv and Mg-pv. We are not aware of any

50 studies of the physical properties of a Ca-Mg-pv phase but first it is important to establish whether this phase
51 can exist in the mantle.

52 The solubility of Ca in Mg-pv and Mg in Ca-pv has been previously studied, and it is generally found
53 that these two phases have very limited mutual solubility under lower mantle conditions (Armstrong et al.
54 2012; Fujino et al. 2004; Irifune et al. 2000; Irifune et al. 1989; Jung and Schmidt 2010; Muir et al. 2021;
55 Tamai and Yagi 1989; Vitos et al. 2006). This limited solubility is speculated to be due to the large size
56 difference between Mg^{2+} and Ca^{2+} , which could reduce the miscibility (Jung and Schmidt 2010; Kesson et al.
57 1995; Vitos et al. 2006). As the lower mantle is more Mg rich than Ca rich, we shall focus on the solubility of
58 Ca in Mg-pv. Experimentally Irifune et al. (1989) found that the solid solubility of Ca in Mg-pv was limited
59 to 2% or even lower at 25 GPa and ~1800 K. Armstrong et al. (2012) found that at 2000 K, the solubility of
60 Ca in Mg-pv is less than 5% at 30 GPa and at least 10% at 55 GPa. With increasing pressure, the solubility
61 thus increases. Theoretically Jung and Schmidt (2010) found that the solubility of Ca in Mg-pv was 0.5% at
62 25 GPa and 2000 K, but 5% at 25 GPa and 3000 K, and Vitos et al. (2006) claimed that under the temperature
63 and pressure conditions of the upper mantle and transition zone, the solid solubility of Ca in Mg-pv is 4-6%.
64 Jung and Schmidt (2010) and Vitos et al. (2006) found that pressure decreased the solid solubility of Ca in
65 Mg-pv in contrast with experimental findings (Armstrong et al. 2012). This was rectified by our recent study
66 (Muir et al., 2021) where we found that the explicit inclusion of vibrational entropy caused pressure to
67 increase miscibility; the results demonstrated that above the D'' in the lower mantle, pyrolytic compositions
68 of Mg-pv and Ca-pv will not mix. Thus, all previous studies agree that pure Ca-pv and Mg-pv will not mix in
69 pyrolytic compositions in lower mantle except possibly in deep hot parts of the lower mantle.

70 Defect elements, such as Fe, Al, and Ti may, however, play important roles in the mixing of these
71 phases. Creasy et al.(2020) recently found that a pyrolytic mixture with around 1-5% Fe in the bridgmanite

72 formed two distinct perovskite phases, Mg-pv and Ca-pv, at lower mantle conditions (up to 75 GPa and 2300
73 K) when it was reduced (pure ferrous iron) but one single phase when half of the iron was oxidized to ferric
74 iron. Armstrong et al. (2012) clearly pointed out that the addition of titanium will enlarge the single phase
75 domain of MgSiO₃-CaSiO₃. Using *ab-initio* calculations we previously established (Muir et al., 2021) a
76 simple conceptual model to explore the influence of different impurities on the miscibility of Ca-pv and
77 Mg-pv and found that large amounts of any defect element (>~1%) were required to significantly affect
78 miscibility. This model had numerous omissions, however, and needs to be extended for any relevant
79 element. Iron is the most prominent defect element in pyrolytic compositions and thus is a key candidate for
80 potentially changing the dynamics of this phase mixing. In the lower mantle, iron concentration in
81 bridgmanite is around ~10% (Irifune et al. 2010), and it may be even higher near the Core Mantle Boundary
82 (CMB). Fujino et al. (2004) explored the effect of iron on the perovskite two-phase mixing using laser heated
83 DAC and TEM. They found that the solid solubility of Mg in Davemaoite was 4% at ~30 GPa and 1930 K
84 but increased to ~18% at 30 GPa and 1800 K when around 9% iron was added which shows clearly that iron
85 promotes miscibility at least to some degree. In Creasy et al.(2020) samples with 27% davemaoite and
86 around 3% ferrous iron in the bridgmanite were not mixed up to 75 GPa and 2300 K which suggests that the
87 solubility is below this point. In both studies there are not enough P, T and Fe% points to explore
88 systematically the effect of iron on the miscibility of the two perovskites. In this study, we conduct
89 theoretical calculations to examine the effect of iron concentration, pressure (P) and temperature (T) on the
90 mutual solubility of Ca-pv and Mg-pv at the lower mantle conditions.

91 Specifically, we examine how varying the Ca and the Fe content of bridgmanite and davemaoite
92 mixtures affects their solubilities. We shall thus define two terms Ca% which is $\text{Ca} / (\text{Mg} + \text{Ca} + \text{Fe}) \times 100\%$,
93 and Fe%, which is $\text{Fe} / (\text{Mg} + \text{Ca} + \text{Fe}) \times 100\%$. The calcium content varies in different compositions that can

94 occur in the lower mantle. The Ca% of mid-ocean ridge basalt (MORB) is between 30-60% (Hirose 2002;
95 Hirose et al. 2005; Ricolleau et al. 2010), of harzburgitic compositions about 1-3% (Michael and Bonatti
96 1985; Ringwood 1991), and of pyrolytic compositions around 7-13% (Kesson et al. 1998; Mattern et al.
97 2005; Ringwood 1991). Iron in the lower mantle can have multiple oxidation states (primarily +2 and +3)
98 and structural sites (A and B) (Gialampouki et al. 2018; Muir and Brodholt 2020; Wang et al. 2019). To
99 determine the effect of iron on A site mixing of Ca and Mg, we shall focus on ferrous iron at the A site. This
100 is likely also the predominant oxidation state of iron across the lower mantle in the absence of Aluminum
101 (Wang et al. 2019). The iron content of Bridgmanite in the lower mantle is about 10% (Irifune et al. 2010),
102 but maybe lower or higher in some regions and so we shall study iron concentrations of 0-25%. While the
103 iron concentration of bridgmanite may be low in the presence of ferropericlase, the formation of a mixed
104 perovskite phase may increase the favorability and thus the concentration of iron in perovskite structures and
105 this favorability needs to be examined. Ferrous iron in bridgmanite is in a state of high spin (Shim et al. 2017;
106 Shukla et al. 2015; Xu et al. 2015) under mantle pressures and temperatures and so all of our calculations will
107 have iron fixed to the high spin state.

108 **Methodology**

109 **Computational Details**

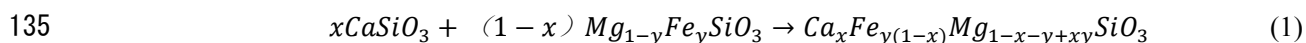
110 The simulations were carried out by VASP (Kresse and Furthmuller 1996a; Kresse and Furthmuller
111 1996b) using the projector-augmented-wave (PAW) method (Kresse and Joubert 1999) and the PBE
112 formulation of GGA (Perdew et al. 1996; Perdew et al. 1997). In all calculations, the following PAW
113 potentials were used: Core region cut-offs are 2.3 atomic units (a.u.) for calcium (core configuration $1s^2 2s^2 p^6$,

114 $3s^23p^64s^2$ as valence), 1.9 a.u. for silicon (core configuration $1s^22s^22p^6$, $3s^23p^2$ as valence), 1.52 a.u. for
115 oxygen (core configuration $1s^2$, $2s^22p^4$ as valence), 2.0 a.u. for magnesium (core configuration $1s^22s^2$, $2p^63s^2$
116 as valence) and 2.3 a.u. for iron (core configuration $1s^22s^22p^63s^23p^6$, $3d^74s^1$ as valence). Traditional DFT
117 does not deal well with heavily correlated electrons such as the d electrons of Fe, and so some kind of
118 correction is needed to capture their electron energy levels accurately. For this, the Hubbard U approach and
119 the rotationally invariant formulation of GGA+U introduced by Dudarev et al. (1998) was used, where an
120 additional localized energy penalty is introduced for intra-atomic interactions, in this case for 3d electrons in
121 Fe. The empirical value of U_{eff} (U-J) was set to be 2.5 eV.

122 A unit cell of 40 atoms was used in static calculations (except for 6.25% Fe where 80 atom unit cells
123 were used) and one with 80 atoms ($2 \times 2 \times 1$) in Molecular dynamics (MD) simulations. In our calculations,
124 $\text{Mg}_{1-x}\text{Fe}_x\text{SiO}_3$ and $\text{Mg}_{1-x-y}\text{Fe}_x\text{Ca}_y\text{SiO}_3$ were modelled with an orthorhombic (*Pbnm*) unit cell. We also
125 calculated *I4/mcm* and *Pm3m* structures for $\text{Mg}_{1-x-y}\text{Fe}_x\text{Ca}_y\text{SiO}_3$ but they were found to be less stable than a
126 *Pbnm* structure at all P and T conditions. For CaSiO_3 both *I4/mcm* and *Pm3m* structures were modelled with
127 *Pm3m* favoured at high temperatures. Calculations were done at 25, 75 and 125 GPa (all pressures are
128 uncorrected) and at 0 (static), 1000, 2000 and 3000 K (molecular dynamics). Static simulations (~ 0 K) were
129 calculated with a $(3 \times 5 \times 5)$ k-point mesh ($4 \times 4 \times 4$ for 6.25 Fe% iron), and molecular dynamics runs were
130 conducted at the gamma point only. Both static and MD calculations had an energy cutoff of 500 eV and
131 were converged to within 10^{-5} eV. Molecular dynamics were performed in an NVT ensemble with the Nosé
132 thermostat and fluctuations around 20 THz and energies were determined from a run of 2.5 ps.

133 **Mixing Thermodynamics**

134 In order to find the solubility of CaSiO_3 in $(\text{Mg}, \text{Fe})\text{SiO}_3$, we examined the following reaction:



136 The iron is placed in Mg-pv before mixing is simulated. Although some iron must thermodynamically enter
137 into Ca-pv as discussed in the text this amount is generally negligible and can be ignored. To determine
138 mixing we calculate the free energy of Reaction 1 using

139
$$G_{Mix} = H_{Mix} - TS_{Mix} \quad (2)$$

140 where $G_{Mix} = 0$ represents the mixing boundary, and mixing occurs when G_{Mix} of Equation 1 is negative. T_{Mix}
141 is the mixing temperature defined as the T which makes $G_{Mix} = 0$ (*i.e.* the solvus temperature). H_{Mix} is the
142 mixing enthalpy. Determining S_{Mix} (the mixing entropy) is complex; in our case we have defined it as the
143 sum of configurational and vibrational entropies.

144 For the configurational entropy, for each specific calcium and iron content in the unit cell we calculated
145 the relative enthalpy of different configurations of Fe, Ca, and Mg where a configuration is the arrangement
146 of Fe, Ca and Mg across the A lattice sites. We then used this equation (Gibb's entropy equation) to calculate
147 S_{Config} :

148
$$S_{Config} = -k_b \sum_i \frac{1}{\sum_i e^{\frac{-E_i}{k_b T}}} e^{\frac{-E_i}{k_b T}} \ln \frac{1}{\sum_i e^{\frac{-E_i}{k_b T}}} e^{\frac{-E_i}{k_b T}} \quad (3)$$

149 where k_b is Boltzmann's constant, T is temperature and E_i is the relative energy of each configuration.
150 Strictly speaking S_{config} should be determined with the relative energy of each configuration including their
151 high temperature components. Practically the difference in phonons between different configurations should
152 be small particularly if their relative enthalpy is small which is indicative of no large structural
153 rearrangements. As outlined in the text we find enthalpy differences between different arrangements to not
154 be large. Thus, we shall use the relative enthalpy in each case when calculating using Equation 3. The
155 number of theoretical arrangements in each case is $Z = \frac{N!}{N_{Mg}! * N_{Ca}! * N_{Fe}!}$ (N is the sum of Mg, Ca and Fe).

156 To calculate configurational entropy, we calculated the relative enthalpy of all possible arrangements of

157 Fe, Ca and Mg in our 40 atom unit cells when these atoms were confined to relaxed A lattice sites. This was
158 done with Ca%=0, 12.5, 25, 37.5, 50, 62.5, 75 and 100 and with 0, 1 or 2 irons (Fe%=0, 12.5 and 25%) at 25,
159 75 and 125 GPa with the solutions to Equation 2 given in Table S1. In addition, we calculated the “perfect”
160 entropy which is the entropy if all arrangements had the same energy, the Boltzmann entropy. This is done
161 via $S_{\text{config}} = k_b \ln Z$ where Z is the total number of arrangements of all atoms as outlined above. We found that
162 the difference between the two calculation methods is very small. Therefore, our configuration entropy for
163 mixing in this study was calculated by the formula $S_{\text{config}} = k_b \ln Z$ and the more detailed results in Online
164 Material¹ Table S1 were ignored.

165 For vibrational entropy (S_{vib}), we obtain the velocity autocorrelation function through molecular
166 dynamics calculations. The vibrational entropy is then determined by:

$$167 \quad S(v) = \frac{2}{k_b T} \sum_{i=1}^N \sum_{k=1}^3 m_a s_a^k \quad (4)$$

$$168 \quad S_{\text{vib}} = k_b \int_0^\infty S(v) dV \quad (5)$$

169 where N is the number of atoms in the system, m_a is the mass of atom a , s_a^k is the spectral density of atom a
170 in the direction k ($x=1, y=2, z=3$) and V is the velocity. Errors were assessed using the Flyvbjerg technique
171 (Flyvbjerg and Petersen 1989) and were < 1.5 meV/atom in all cases. We propagated these errors in Figure
172 5 and find that due to the similar energy of the mixed and unmixed phase even this small error can add +/-
173 ~ 100 K to the mixing temperature.

174 To determine partitioning between two phases we first determined G of each phase as a function of
175 iron content. This was done through plotting the variation in H_{mix} and S_{vib} with our calculated points and
176 fitting polynomials and through the analytical form of S_{Config} . For a fixed amount of iron we then
177 partitioned iron between the two phases until G was minimized.

178 In summary for any condition (Ca%, Fe%, P) the mixing temperature is determined as such. We first
179 calculated the enthalpy of mixing at a set pressure. For 0% iron content this was done in 40 atom unit cells
180 at 0/12.5/25/37.5/50/62.5/75/82.5 and 100 Ca% content. For 6.25% iron content this was done in 80 atom
181 unit cells at 0/12.5/25/50 and 100 Ca% content. For 12.5% iron content this was done in 40 atom unit cells
182 at 0/6.25%/12.5%/25%/50%/75% and 100% Ca% content. For 25% iron content this was done in 40 atom
183 unit cells at 0/6.25%/12.5%/25%/62.5% and 100% Ca% content. Before mixing iron was partitioned into
184 its favored phase, Mg-pv (see text), we extrapolated the mixing enthalpies using second-order polynomials
185 across first Ca%, then Fe% and then pressure to determine enthalpies at points beyond this. The
186 configurational entropy of mixing was then determined at a set composition using the Boltzmann entropy
187 (which is insensitive to pressure) at the required temperature. Vibrational entropy was added using the
188 results of iron free systems as outlined in our recent study (Muir et al., 2021) with the contribution of iron
189 to vibrational entropy ignored as explained earlier. Configurational and vibrational entropy was added to
190 the mixing enthalpies and the temperature varied until Equation 1 equals 0.

191

192 **Results & Discussion**

193 **Fe Partitioning**

194 The partitioning of ferrous iron (K_D) between different possible phases (Ca-pv, Mg-pv and the mixed
195 phase) will be a strong control on perovskite phase mixing and thus must be first considered. If ferrous iron is
196 strongly favoured in the mixed phase this will increase the favorability of phase mixing and vice versa. The
197 strength of partitioning will also determine some of the dynamics of phase mixing. For example, a strong

198 preference for ferrous iron to enter the mixed phase would lead to a wide phase loop whereas a weak
199 favorability would lead to a narrow phase loop. A strong preference for ferrous iron to enter the mixed phase
200 could also lead to a mechanism by which iron-rich regions of the mantle could phase mix and become
201 dynamically separated from the rest of the mantle.

202 In the lower mantle a third phase is present, that of ferropericlase. In a pure Ca-free bridgmanite ferrous
203 iron prefers ferropericlase over bridgmanite (Muir and Brodholt, 2016)). On the surface the presence of Ca
204 should not change this preference and thus it could be considered that bridgmanite in the lower mantle is
205 iron-free and that we could ignore the effect of iron on mixing altogether. This story will change, however, if
206 the presence of Ca enables the formation of a mixed phase into which ferrous iron prefers to partition over
207 both bridgmanite and ferropericlase and thus we shall examine whether this is likely to be the case. Such an
208 effect could change distribution of iron across the lower mantle as a whole. A likely pathway for this effect
209 would be A) iron rich bridgmanite + iron poor ferropericlase \rightarrow iron poor bridgmanite + iron rich
210 ferropericlase \rightarrow iron poor mixed phase + iron rich ferropericlase \rightarrow iron rich mixed phase + iron poor
211 ferropericlase. Pathway B) iron rich bridgmanite \rightarrow iron rich mixed phase is thermodynamically identical to
212 pathway A if they both run to completion and thus shall be calculated here though pathway A is more likely
213 in a real mantle.

214 We consider two Fe partitioning coefficients, one between MgSiO_3 and CaSiO_3 ($K_{D1}^{\text{Fe}} = X_{\text{Fe}}^{\text{Mg-pv}} /$
215 $X_{\text{Fe}}^{\text{Ca-pv}}$) and one between MgSiO_3 and $(\text{Mg}_{1-x}\text{Ca}_x)\text{SiO}_3$ ($K_{D2}^{\text{Fe}} = X_{\text{Fe}}^{\text{Mg-pv}} / X_{\text{Fe}}^{(\text{Mg}_{1-x}\text{Ca}_x)\text{SiO}_3}$). In both cases we
216 only consider ferrous iron and a value above 1 means iron prefers bridgmanite over the alternative. Some
217 values for these are given in Table 1 and Figure 1. K_{D1} considers a case where Ca-pv partitions iron out of
218 bridgmanite and that interferes with Pathway A or B. We find that K_{D1} is always >1 and that Fe^{2+} always
219 prefers to partition into Mg-pv over Ca-pv. Thus Ca-pv can be considered as an iron-free phase and in a

220 Mg-pv and Ca-pv mixture all iron shall be considered partitioned into Mg-pv as in Reaction 1. For a few
221 systems we tested the effect of including K_{D1} partitioning and allowed iron to partition into both davemaioite
222 and bridgmanite before forming a perovskite mixed phase but we found no substantial changes (<20 K,
223 generally below <5 K) to our values of T_{mix} . K_{D2} calculates partitioning of Fe^{2+} across pathway B. We find
224 that except for very large amounts of Fe^{2+} at low pressures (where mixing is not expected to occur), Fe^{2+}
225 always favors the mixed phase over Mg-Pv ($K_{D2} < 1$) and that this preference increases with pressure. The
226 amount of Fe^{2+} in the system has an effect on the value of K_{D2} but this is small as shown in Figure 1. In no
227 cases at high pressure (where mixing is likely to occur) does Fe^{2+} favor bridgmanite over the mixed phase.
228 This preference is not particularly strong, however, with all K_{D2} values being above 0.25 excepts in cases
229 with extreme iron contents or in a basaltic mixture.

230 As discussed above Fe^{2+} could potentially partition from bridgmanite either to ferropericlase or to the
231 mixed phase. We can examine this by comparing our K_{D2} values for Fe^{2+} going from bridgmanite to the
232 mixed phase to calculated K_D values of Fe^{2+} going from bridgmanite to ferropericlase. Muir and Brodholt
233 (2016) claimed that there is a strong partitioning of ferrous iron from bridgmanite to ferropericlase with a K_D
234 of ~0.32 at 30 GPa dropping to ~0.06 at 120 GPa at 2000 K and dropping further with increased temperature.
235 This is a much stronger preference for ferrous iron going into ferropericlase than into the mixed phase and so
236 the preference of ferrous iron at deep mantle pressures and temperatures where mixing occurs is
237 ferropericlase > the mixed phase > bridgmanite in that order. Thus, the formation of a perovskite mixed
238 phase does not outcompete ferropericlase as an iron-sink and should not substantially alter the distribution of
239 iron in the deep lower mantle. Phase mixing is thus not a way to produce iron-rich regions in the lower
240 mantle. Our concentrations of iron in the rest of this paper shall refer to the concentration of ferrous iron in
241 the perovskite phases (bridgmanite and the mixed phase). In a real lower mantle with ferropericlase this

242 concentration will be lower than the concentration of iron in the system and could be up to 20 times lower as
243 you approach the CMB (Muir and Brodholt, 2016)).

244 **Effect of Iron on Mixing Energies**

245 In this section we shall examine the effect of ferrous iron on the individual energetic components of mixing.

246 H_{Mix}

247 We determined the effect of ferrous iron on the mixing enthalpy $\{\{\text{auth: ok? Elsewhere?}\}\}(\Delta H_{Mix})$
248 using static DFT calculations with the results shown in Figure 2 (and more data is presented in Table S2).
249 H_{Mix} is always positive which shows that Ca-pv and Mg-pv are naturally immiscible and that temperature is
250 required to mix them. With increasing pressure H_{Mix} increases which will lead to a decrease in the
251 favorability of mixing. Fe^{2+} in general decreases H_{Mix} and thus promotes phase mixing but this trend is
252 nonlinear with iron concentration. Initially H_{Mix} decreases with an increasing iron concentration but after a
253 specific iron concentration is reached H_{Mix} then increases with increasing iron concentration. The reason for
254 this nonlinearity can be seen in Figure S1, which plots the change in energy of $Mg_{1-x}Fe_xSiO_3$ and
255 $Mg_{1-x-y}Fe_xCa_ySiO_3$ as a function of Fe^{2+} concentration. Replacing Mg with Fe has a similar effect on the
256 enthalpies of the mixed phase and Mg-pv as both structures are extremely similar. Hence, the effect of iron
257 on the enthalpy difference between these two systems is highly sensitive to small structural relaxations and
258 thus deviations from linearity are seen. Such deviations grow larger as the iron concentration increases and
259 both mixed and unmixed structures begin to transition to an iron-rich end member which has significant
260 structural and energetic differences to the Mg-rich end-member. While the effect of substitutional defects on
261 properties like enthalpy are generally linear with concentration, these defects are usually present in much

262 smaller concentrations than are seen for Fe in bridgmanite. At high defect concentrations (such as above ~10%
263 Fe²⁺) defect-defect interactions are significant and can cause nonlinear deviations to H_{MIX} when the enthalpy
264 difference between the starting and ending products are small. It is important to stress that for structures
265 considered in our reactions and for each Ca% and Fe% considered we calculated the enthalpy of all possible
266 configurations of Fe, Ca and Mg in our models and used the lowest enthalpy. Thus this nonlinear trend is not
267 an artefact of the favored arrangement of iron in these systems changing with concentration. The relative
268 enthalpy of different iron configurations with a fixed composition can vary by up to 0.15 eV/f.u. and so is
269 similar to the energy difference between unmixed and mixed phases.

270 S_{Config}

271 We examined the effect of different iron arrangements, as explained in the methods, to estimate the
272 effect of iron on configurational entropy (S_{Config}) of end members and mixed systems. In a perfect system
273 (where all arrangements of atoms are energetically equivalent) the presence of iron does not cause an
274 increase to S_{Config} during mixing. This is because iron exists on the A site where mixing between Mg and Ca
275 occurs in the perfect system and because iron is primarily partitioned to a single phase before mixing. As
276 shown in Table S1, the configurational entropy of the both iron-bearing Mg-pv and the Fe,Mg,Ca bearing
277 mixed phase is near the perfect Boltzmann entropy limit. At all conditions, the difference between a perfect
278 Boltzmann configurational entropy and our calculated configurational entropy is $< \sim 4$ meV/atom. This is a
279 very small energy term and is much smaller than the H_{MIX} term. This suggests that all arrangements of Mg, Fe
280 and Ca on the A sites in both Mg-pv and the mixed phase are effectively equivalent and that iron does not
281 cause large structural rearrangements in Mg-pv or the mixed phase. This means that the effect of iron on the
282 configurational entropy of mixing can largely be approximated by considering it as an ideal system. In other

283 words, iron does not cause an increase in mixing S_{Config} and does not promote mixing in this way.
284 Considering a system with 12.5% Fe and 12.5% Ca, changing between perfect and non-perfect S_{Config}
285 changes the mixing temperature by ~ 50 K. Thus, the primary effect on iron on mixing should be enthalpic
286 and effect of iron on S_{config} can largely be ignored. These results are a vindication of one of the assumptions
287 in the model of Muir et al. (2021) where S_{config} was treated using the perfect Boltzmann limits.

288

289 S_{Vib}

290 Vibrational entropy (S_{Vib}) depends on long-range phonons and is likely unaffected by the addition of
291 defects in small concentrations but could be strongly affected by defects present in large quantities like Fe.
292 S_{Vib} is essential to calculating mixing parameters of these systems (Muir et al., 2021) but we predict that
293 $\Delta S_{\text{Vib-Fe}}$ (the change caused to S_{Vib} by iron) is not essential. Iron makes no large structural rearrangements to
294 the system as indicated by its near-perfect values of S_{config} and thus likely also has small effects on long range
295 vibrational entropy. The change in the vibrational entropy term from replacing a Mg atom with an iron atom
296 is calculated to be extremely small (Table 2), particularly at high pressures where mixing occurs. With the
297 conditions in Table 2 including an $\Delta S_{\text{Vib-Fe}}$ term changes T_{mix} at 25 GPa by <50 K but by <0.5 K at 125 GPa
298 at conditions where mixing occurs. Therefore, in this work we shall include S_{Vib} but ignore the effects of
299 $\Delta S_{\text{Vib-Fe}}$. These results are a vindication of one of the assumptions in the model of Muir et al. (2021) where
300 $\Delta S_{\text{Vib-X}}$ was ignored when introducing defect elements.

301 **Mixing**

302 Previously the mixing of iron-free forsterite was explored and compared with experimental results in
303 Muir et al. (2021). In that work it was found that a pyrolytic mixture of pure Mg-pv and Ca-pv will not mix
304 along normal geotherms before the D'' layer. In this work we shall focus on how iron could change this
305 picture.

306 In Figure 3, we plot the T_{mix} of a 1:7 (pyrolytic) mixture of davemaioite and Bridgmanite as a function of
307 iron at pressures of 25, 75 and 125 GPa. When iron is initially added into the system the mixing temperature
308 decreases by about 80 K per 1% Fe. This T_{mix} decrease in a pyrolytic mixture does not continue universally
309 with concentration, however, and a T_{mix} minimum is seen at ~13% Fe. Beyond this increasing the ferrous
310 iron concentration causes T_{mix} to rise. Overall this means that while a small amount of iron (6.25%) causes a
311 T_{mix} decrease of 500 K a large amount of iron (25%) causes a much smaller decrease in T_{mix} (<100 K). As
312 shown in Figure 2, the Fe induced decrease in H_{Mix} is largest at ~13% and is smaller at either side of this.

313 Figure 3 also shows the effect of iron on a 1:1 mixture of Ca-pv and Mg-pv (Ca%=50, basaltic). In this
314 case, unlike the pyrolytic case, T_{mix} decreases with increasing iron concentration continually up until 25%. A
315 likely explanation for the different behaviors between pyrolytic and basaltic compositions is due to iron
316 partitioning preferences. The iron partitioning coefficient (K_{D1}^{Fe}) between MgSiO_3 and CaSiO_3 is generally
317 large, with strong partitioning of Fe into the Mg end-member. The iron partition coefficient (K_{D2}^{Fe}) between
318 bridgmanite and the mixed phase is smaller and closer to 1, particularly at lower pressures. Thus, there is a
319 strong dislike of Fe going into Ca sites rather than Mg sites as Fe^{2+} is much closer in size to Mg^{2+} than it is to
320 Ca^{2+} (~78/72/100 pm respectively). At low ferrous iron concentrations iron partitions into the mixed phase
321 and thus reduces the mixing temperature. As iron concentration increases relative to Ca concentration, iron
322 will partition into the Mg-end member and not take part in the miscibility process. Thus, it will cost energy to

323 put the surplus iron back into the mixture (T_{mix} increase). The iron concentration at which a T_{mix} decrease is
324 converted into a T_{mix} increase (the T_{mix} minimum) depends upon the relative amount of Fe sites vs Ca sites.
325 When Ca% is 12.5% (pyrolytic mixture), the iron-driven two-phase solid solution T_{mix} minimum is around
326 13% Fe but when Ca% is 50% (basaltic mixture) this T_{mix} minimum increases to ~30% Fe.

327 Figure 4 presents the solubility of CaSiO_3 and MgSiO_3 with different amounts of iron at a deep lower
328 mantle pressure (125 GPa). In low-iron, moderate-iron and iron-free systems solubility rises sharply with
329 temperature when Ca% is low before reaching a plateau where solubility rises much slower with temperature.
330 In high-iron system solubility has much more complex effects with Ca% due to the rising incompatibility of
331 Fe and Ca as discussed above. Thus at deep pressures T_{mix} is similar for a pyrolytic (Ca%=12.5 2518 K) and
332 a basaltic (Ca%=50% 2593 K) composition in the absence of iron. With the introduction of moderate
333 amounts of iron 6.25%/12.5% iron this harmony is maintained as T_{mix} reduces to ~2280 K/~2180 K for the
334 pyrolytic mixture and ~2290 K/2040 K for the basaltic mixture, respectively. The introduction of a large
335 amount of iron (25% Fe), however, causes T_{mix} to vary wildly between the pyrolytic (~2520 K) and basaltic
336 (~1850 K) compositions.

337 The most direct experimental measurement of the effect of iron on T_{mix} comes from Fujino *et al.* (2004).
338 Comparisons with that work are difficult, however, due to the high concentrations of Fe in their samples
339 (with Fe nearly equivalent to Mg) and due to its focus on the Ca-pv side of the solubility diagram. As
340 discussed above, the behavior of solubility in the presence of high iron concentrations is not easy to predict
341 and the concentrations of iron in Fujino *et al.* (2004) are beyond the scope of our calculations. Nevertheless,
342 our study is consistent with the findings of Fujino *et al.* (2004) in that iron can promote the miscibility of two
343 perovskite phases. A comparison can also be made with Creasy *et al.* (2020). In the presence of pure ferrous
344 iron, mixing was not seen in a sample with 27% Ca that was placed under pressure from 35-75 GPa and

345 heated up to 2300 K. At 75 GPa we predict T_{mix} for this system to be 2942 K with 3% ferrous iron and 2850
346 K with 5% ferrous iron and thus we also predict that these phases should not mix.

347 The effect of ferrous iron concentration on T_{mix} is thus strongly non-linear. This is very different from
348 the simple model presented in Muir et al. (2021) which assumed a linear effect of ferrous iron concentration
349 on T_{mix} . This non-linearity is largely due to non-linear variations in H_{Mix} and stresses the importance of fully
350 calculating the effect of defective elements rather than simple extrapolations. The model in Muir et al. (2021)
351 is thus generally valid at low iron concentrations but overestimates the effect of Fe on T_{mix} at high iron
352 concentrations. This leads to quite different implications as the simple linear model would state that high
353 iron systems are extremely likely to have perovskite phase mixing in the mantle and could segregate iron
354 from the regular mantle but as we demonstrate here high iron systems are actually less likely to have
355 perovskite phase mixing than low iron systems.

356 When considering other defect elements the simple linear concentration model of Muir et al. (2021) is
357 more likely to apply than it does to iron. There are two reasons. First, iron has very large concentrations in
358 bridgmanite whereas most defective elements have smaller concentrations. Non-linear modifications to
359 H_{Mix} are more likely as the concentration of defects increases. Below ~10% ferrous iron non-linear
360 modifications to H_{Mix} are small and the linear model of Muir et al. (2021) and the model presented here
361 predict very similar T_{mix} values. Most defective elements in bridgmanite will have concentrations much
362 lower than this and thus H_{Mix} is expected to behave linearly with the concentration of the defect. The second
363 reason is that Fe^{2+} and Mg^{2+} are very similar and thus replacing Mg^{2+} with Fe^{2+} causes very small structural
364 distortions in both bridgmanite and the mixed phase. This leads to the effect of iron on H_{Mix} to be small and
365 thus varying the concentration of iron does not cause large effects on H_{Mix} . As defective elements become
366 more dissimilar to those found in bridgmanite they will induce larger structural distortions to bridgmanite

367 and the mixed phase and thus will induce larger changes to H_{Mix} which will be much more linearly dependent
368 on defect concentration. Thus other defective elements are speculated to have much more linear effects on
369 H_{Mix} with varying defect concentration and to be much closer to the linear model found in Muir et al. (2021).

370 We shall now explore how iron could affect mixing of a pyrolite across the lower mantle. Figure 5
371 presents the T_{mix} of a pyrolytic mixture ($\text{Ca}\%=12.5$) as a function of depth and iron concentration.
372 Regardless of the amount of iron no mixing is predicted at the top of the lower mantle. With the
373 concentration of iron that causes the maximum favorability of mixing ($\sim 13\%$) perovskite phase mixing is
374 predicted to occur at ~ 70 GPa in the hottest parts of the mantle. As the iron concentration increases or
375 decreases or the mantle cools then mixing only occurs at deeper parts of the mantle. A ferrous iron
376 concentration of 13% would be an extremely iron rich part of the mantle, especially when considering the
377 effects of ferropericlase, and more reasonable perovskite iron concentrations lie between 0-6.25%. With
378 these iron concentrations and the “standard” geotherm, mixing is predicted to occur between 115-125 GPa
379 depending upon the iron concentration. Thus, in a pyrolytic mantle ferrous iron causes only very small
380 changes to the depth at which phase mixing is predicted to occur and the concentration of iron is not a large
381 control on this process. Temperature fluctuations would be a much stronger control. Similar observations can
382 be made with a basaltic composition (Figure S2) but in this case the higher value of $\text{Ca}\%$ means no phase
383 mixing is predicted to occur under any conditions.

384 Iron-rich regions present an interesting case. Various regions, particularly those near the CMB, have
385 been speculated to be iron rich and these could present quite different behavior from the rest of the mantle.
386 We find however that large amounts of iron decrease the stability of the mixed phase and do not promote its
387 formation. Thus, these regions would not have different phase mixing characteristics from the rest of the
388 iron-poor mantle. The potential formation of a mixed phase also does not provide a mechanism for forming

389 iron rich regions. A strong partitioning of iron from bridgmanite to the mixed phase could provide a physical
390 mechanism for dynamically separating iron from the overall mantle across the physical barrier of a phase
391 transition but the partitioning coefficient of ferrous iron between bridgmanite and the mixing phase is small
392 (Table 1) and moves closer to 1 with increasing iron (Figure 1) and thus this mechanism is unlikely.

393 So far, we have considered only univariant mixing but the introduction of iron will lead to a phase
394 loop. Calculating the exact dimensions of this phase loop is challenging. The similar trends of formation
395 enthalpies vs Fe% for Mg-pv and the mixed phase (Figure S1), and their highly variable relationship to
396 each other mean that constraining the phase loop requires very high accuracy in both the number of Fe
397 concentrations that are measured and the precision of those points. This is potentially important future
398 work but the phase loop is unlikely to be large or important simply due to K_{D2} being near 1. A wide phase
399 loop would require strong partitioning of the iron to either Mg-pv or the mixed phase. Using a common
400 tangent method, we calculate that at 125 GPa the width of the phase loop is < 200 K at 6.25% Fe and < 50
401 K at 12.5% Fe (both with Ca%=12.5), but the method is not well constrained. Regardless it is difficult to
402 propagate a wide phase loop in Fe space for the perovskite mixing reaction due to their close partitioning
403 values and the phase loop must have widths of similar order to what are calculated here.

404 Finally, we consider the effect of other elements. The two other major components we expect to be
405 important in perovskite phase mixing are ferric iron and aluminum. While ferrous iron is expected to be
406 dominant over ferric iron (Xu et al. 2015) in deep lower mantle bridgmanite the presence of Al can convert
407 ferrous iron to ferric iron by making Fe^{3+} - Al^{3+} and Al itself could affect mixing dynamics. The effect of
408 these elements was studied with a simple linear enthalpic model in Muir et al. (2021) where it was
409 concluded that Al raises the mixing temperature and Fe^{3+} - Al^{3+} causes the mixing temperature to remain
410 largely static. While this was a simplistic model it correctly predict the trends seen for Fe^{2+} at low Fe

411 concentrations and thus model likely captures the broad trend of Ferric iron and aluminum in that they
412 have little effect on mixing or slightly raise the mixing temperature. Thus, based on our model the presence
413 of ferric iron and Al will likely not increase the favorability of phase mixing and our predictions above
414 reflect conditions of maximum solubility. This effect is in contrast to Creasy et al.(2020) where an increase
415 in ferric iron was predicted to increase mixing such that no mixing was seen with ferrous iron (as we also
416 predict under their conditions) but mixing was seen with ferric iron. Determining the exact nature of these
417 effects is complicated in that the oxidized sample in this work also had increased total iron (which
418 increases mixing at these low temperatures) and a larger amount of Al in its sample (as higher ferric iron
419 allows more Al to be adsorbed) which changes the dynamics significantly. It should be noted that these
420 experiments lacked ferropericlasite which may partition out the iron in a real mantle. The presence of ferric
421 iron (either in Fe-Fe or Al-Fe pairs) leads to an increase in S_{conf} upon mixing so would be expected to
422 increase the favorability of perovskite phase mixing but in the model of Muir et al. (2021) this effect was
423 opposed by penalties in H_{mix} . The results of Creasy et al.(2020), however, suggest that a simple linear model
424 may not correctly reflect the effect of ferric iron and aluminum in perovskite phase mixing and a more
425 detailed study of these species is required.

426 **Implications**

427 The effect of ferrous iron on the phase mixing of Ca-pv and Mg-pv was investigated. It is found that
428 iron reduces the mixing temperature and increases miscibility but in highly non-linear manners. Low iron
429 contents promote the mixing of these two phases but only to a small degree whereas high iron contents
430 have very little effect on the miscibility of these phases and can even hinder mixing. Ca-pv and Mg-pv
431 should exist as independent phases in the lower mantle, but starting at 75 GPa in iron-rich hot mantle they

432 can form a single phase. As iron content decreases or the mantle cools the pressure of this transition
433 deepens to around 120 GPa for a mantle at normal temperatures with a small amount of iron (~1% Fe in
434 the perovskite). It is unclear what seismic signal would come about through such phase mixing. On phase
435 mixing there is a decrease in density but this decrease is small (always <1% in our examined systems)
436 which would likely prevent any large dynamical effects but the seismic properties of the mixed phase are
437 unknown so we cannot compare them to proposed lower mantle heterogeneities such as LLSVPs though
438 this would be useful work for the future. There is weak partitioning of iron from bridgmanite to the mixed
439 phase but this is less favorable than partitioning Fe from bridgmanite to MgO and thus this is not expected
440 to have strong dynamical consequences. Iron may not be a significant factor in determining the phases of
441 the lower mantle as while moderate amounts of iron can drive significant mixing, it is more favorable for
442 iron to exist in ferropericlase than the mixed phase and there is no strong thermodynamic gradient to push
443 iron into a mixed phase where it could be trapped in a dynamic mantle.

444

445 **Acknowledgement**

446 This work was supported by National Natural Science Foundation of China (41773057, 42050410319),
447 with computational re-sources from Computer Simulation Labs of IGGCAS, the National Supercomputer
448 Centers in Shenzhen and Beijing, China.

449

450 **References**

451 Anderson, O.L., Isaak, D.G., and Yamamoto, S. (1989) Anharmonicity and the equation of
452 state for gold. *Journal of Applied Physics*, 65, 1534-1543. doi:10.1063/1.342969
453 Armstrong, L.S., Walter, M.J., Tuff, J.R., Lord, O.T., Lennie, A.R., Kleppe, A.K., and Clark,

- 454 S.M. (2012) Perovskite Phase Relations in the System CaO-MgO-TiO₂-SiO₂ and
455 Implications for Deep Mantle Lithologies. *Journal of Petrology*, 53, 611-635.
456 doi:10.1093/petrology/egr073
- 457 Creasy, N., Girard, J., Eckert, J.O., and Lee, K.K.M. (2020) The role of redox on bridgmanite
458 crystal chemistry and calcium speciation in the lower mantle. *Journal of Geophysical*
459 *Research: Solid Earth*, 125, e2020JB020783 doi:10.1029/2020JB020783
- 460 Dudarev, S.L., Botton, G.A., Savrasov, S.Y., Humphreys, C.J., and Sutton, A.P. (1998)
461 Electron-energy-loss spectra and the structural stability of nickel oxide: An LSDA+U
462 study. *Physical Review B*, 57, 1505-1509. doi:10.1103/PhysRevB.57.1505
- 463 Flyvbjerg, H., and Petersen, H.G. (1989) Error-Estimates on Averages of Correlated Data. *J*
464 *Chem Phys*, 91, 461-466. doi:10.1063/1.457480
- 465 Fujino, K., Sasaki, Y., Komori, T., Ogawa, H., Miyajima, N., Sata, N., and Yagi, T. (2004)
466 Approach to the mineralogy of the lower mantle by a combined method of a
467 laser-heated diamond anvil cell experiment and analytical electron microscopy.
468 *Physics of the Earth and Planetary Interiors*, 143-144, 215-221.
469 doi:10.1016/j.pepi.2003.11.013
- 470 Gialampouki, M.A., Xu, S., and Morgan, D. (2018) Iron valence and partitioning between
471 post-perovskite and ferropericlase in the Earth's lowermost mantle. *Physics of the*
472 *Earth and Planetary Interiors*, 282, 110-116. doi:10.1016/j.pepi.2018.06.005
- 473 Hirose, K. (2002) Phase transitions in pyrolitic mantle around 670-km depth: Implications for
474 upwelling of plumes from the lower mantle. *Journal of Geophysical Research: Solid*
475 *Earth*, 107, ECV 3-1-ECV 3-13. doi:10.1029/2001jb000597
- 476 Hirose, K., Takafuji, N., Sata, N., and Ohishi, Y. (2005) Phase transition and density of
477 subducted MORB crust in the lower mantle. *Earth and Planetary Science Letters*, 237,
478 239-251. doi:10.1016/j.epsl.2005.06.035
- 479 Irifune, T., Miyashita, M., Inoue, T., Ando, J., Funakoshi, K., and Utsumi, W. (2000)
480 High-pressure phase transformation in CaMgSi₂O₆ and implications for origin of
481 ultra-deep diamond inclusions. *Geophysical Research Letters*, 27, 3541-3544.
482 doi:10.1029/2000gl012105
- 483 Irifune, T., Shinmei, T., Mccammon, C.A., Miyajima, N., Rubie, D., and Frost, D.J. (2010)
484 Iron partitioning and density changes of pyrolite in earth's lower mantle. *Science*,
485 5962, 193-195. doi:10.1126/science.1181443
- 486 Irifune, T., Susaki, J., Yagi, T., and Sawamoto, H. (1989) Phase-Transformations in Diopside
487 CaMgSi₂O₆ at Pressures up to 25-Gpa. *Geophysical Research Letters*, 16, 187-190.
488 doi:10.1029/GL016i002p00187
- 489 Jung, D.Y., and Schmidt, M.W. (2010) Solid solution behaviour of CaSiO₃ and MgSiO₃
490 perovskites. *Physics and Chemistry of Minerals*, 38, 311-319.
491 doi:10.1007/s00269-010-0405-0
- 492 Kesson, S.E., Fitz Gerald, J.D., and Shelley, J.M. (1998) Mineralogy and dynamics of a
493 pyrolite lower mantle. *Nature*, 393, 252-255. doi:10.1038/30466
- 494 Kesson, S.E., Fitz Gerald J.D., Shelley, J.M.G., and Withers, R.L. (1995) Phase-Relations,
495 Structure and Crystal-Chemistry of Some Aluminous Silicate Perovskites. *Earth and*
496 *Planetary Science Letters*, 134, 187-201. doi:10.1016/0012-821x(95)00112-P
- 497 Kresse, G., and Furthmuller, J. (1996a) Efficiency of ab-initio total energy calculations for

- 498 metals and semiconductors using a plane-wave basis set. *Computational Materials*
499 *Science*, 6, 15-50. doi:10.1016/0927-0256(96)00008-0
- 500 Kresse, G., and Furthmuller, J. (1996b) Efficient iterative schemes for ab initio total-energy
501 calculations using a plane-wave basis set. *Physical Review B*, 54, 11169-11186.
502 doi:10.1103/PhysRevB.54.11169
- 503 Kresse, G., and Joubert, D. (1999) From ultrasoft pseudopotentials to the projector
504 augmented-wave method. *Physical Review B*, 59, 1758-1775.
505 doi:10.1103/PhysRevB.59.1758
- 506 Mattern, E., Matas, J., Ricard, Y., and Bass, J. (2005) Lower mantle composition and
507 temperature from mineral physics and thermodynamic modelling. *Geophysical*
508 *Journal International*, 160, 973-990. doi:10.1111/j.1365-246X.2004.02549.x
- 509 Michael, P.J., and Bonatti, E. (1985) Peridotite Composition from the North-Atlantic -
510 Regional and Tectonic Variations and Implications for Partial Melting. *Earth and*
511 *Planetary Science Letters*, 73, 91-104. doi:10.1016/0012-821x(85)90037-8
- 512 Muir, J.M.R., and Brodholt, J.P. (2016) Ferrous iron partitioning in the lower mantle. *Physics*
513 *of the Earth and Planetary Interiors*, 257, 12-17. doi:10.1016/j.pepi.2016.05.008
- 514 Muir, J.M.R., and Brodholt, J.P. (2020) Ferric iron in bridgmanite and implications for
515 ULVZs. *Physics of the Earth and Planetary Interiors*, 306, 106505.
516 doi:10.1016/j.pepi.2020.106505
- 517 Muir, J.M.R., Thomson, A.R., and Zhang, F. (2021) The miscibility of Calcium Silicate
518 Perovskite and Bridgmanite: A single phase perovskite in hot, iron-rich regions. *Earth*
519 *and Planetary Science Letters*, 566, 116973. doi:10.1016/j.epsl.2021.116973.
- 520 Ohtani, E., Yuan, L., Ohira, I., Shatskiy, A., and Litasov, K. (2018) Fate of water transported
521 into the deep mantle by slab subduction. *Journal of Asian Earth Sciences*, 167, 2-10.
522 doi:10.1016/j.jseaes.2018.04.024
- 523 Oneil, I. B., and Jeanloz, R. (1990) Experimental Petrology of the Lower Mantle - a Natural
524 Peridotite Taken to 54 Gpa. *Geophysical Research Letters*, 17, 1477-1480. doi:
525 10.1029/GL017i010p01477
- 526 Perdew, J.P., Burke, K., and Ernzerhof, M. (1996) Generalized gradient approximation made
527 simple. *Physical Review Letters*, 77, 3865-3868. doi:10.1103/PhysRevLett.77.3865
- 528 Perdew, J.P., Burke, K., and Ernzerhof, M. (1997) Generalized gradient approximation made
529 simple (vol 77, pg 3865, 1996). *Physical Review Letters*, 78, 1396-1396. doi:
530 10.1103/PhysRevLett.78.1396
- 531 Ricolleau, A., Perrillat, J.-P., Fiquet, G., Daniel, I., Matas, J., Addad, A., Menguy, N., Cardon,
532 H., Mezouar, M., and Guignot, N. (2010) Phase relations and equation of state of a
533 natural MORB: Implications for the density profile of subducted oceanic crust in the
534 Earth's lower mantle. *Journal of Geophysical Research*, 115(B8).
535 doi:10.1029/2009jb006709
- 536 Ringwood, A.E. (1991) Phase-Transformations and Their Bearing on the Constitution and
537 Dynamics of the Mantle. *Geochimica et Cosmochimica Acta*, 55, 2083-2110. doi:
538 10.1016/0016-7037(91)90090-R
- 539 Shim, S.H., Grocholski, B., Ye, Y., Alp, E.E., Xu, S., Morgan, D., Meng, Y., and Prakapenka,
540 V.B. (2017) Stability of ferrous-iron-rich bridgmanite under reducing midmantle
541 conditions. *Proceedings of the National Academy of Sciences*, 114, 6468-6473.

- 542 doi:10.1073/pnas.1614036114
543 Shukla, G., Wu, Z.Q., Hsu, H., Floris, A., Cococcioni, M., and Wentzcovitch, R.M. (2015)
544 Thermoelasticity of Fe²⁺-bearing bridgmanite. *Geophysical Research Letters*, 42,
545 1741-1749. doi:10.1002/2014gl062888
546 Tamai, H., and Yagi, T. (1989) High-Pressure and High-Temperature Phase-Relations in
547 CaSiO₃ and CaMgSi₂O₆ and Elasticity of Perovskite-Type CaSiO₃. *Physics of the*
548 *Earth and Planetary Interiors*, 54, 370-377. doi:10.1016/0031-9201(89)90254-9
549 Vitos, L., Magyari-Köpe, B., Ahuja, R., Kollár, J., Grimvall, G., and Johansson, B. (2006)
550 Phase transformations between garnet and perovskite phases in the Earth's mantle: A
551 theoretical study. *Physics of the Earth and Planetary Interiors*, 156, 108-116.
552 doi:10.1016/j.pepi.2006.02.004
553 Wang, X.L., Tsuchiya, T., and Zeng, Z. (2019) Effects of Fe and Al incorporations on the
554 bridgmanite-postperovskite coexistence domain. *Comptes Rendus Geoscience*, 351,
555 141-146. doi:10.1016/j.crte.2018.10.003
556 Xu, S., Shim, S.H., and Morgan, D. (2015) Origin of Fe³⁺ in Fe-containing, Al-free mantle
557 silicate perovskite. *Earth and Planetary Science Letters*, 409, 319-328.
558 doi:10.1016/j.epsl.2014.11.006
559

560 **Table 1.** The partitioning coefficient of Fe between MgSiO₃ and CaSiO₃ ($K_{D1}^{Fe} = X_{Fe}^{Mg-pv} / X_{Fe}^{Ca-pv}$) and
 561 between Mg_{1-x}Ca_xSiO₃ (x=0.125/0.5) and MgSiO₃ ($K_{D2}^{Fe} = X_{Fe}^{Mg-pv} / X_{Fe}^{(Mg_{1-x}Ca_x)SiO_3}$) at 25 - 125 GPa and
 562 1000 - 3000 K.

	K _{D1}					
	1000 K		2000 K		3000 K	
25 GPa	3.116		1.765		1.461	
75 GPa	6.548		2.559		1.871	
125 GPa	21.815		4.671		2.794	
	K _{D2} (x=0.125)					
	2000 K		2500 K		3000 K	
	6.25%Fe	25%Fe	6.25%Fe	25%Fe	6.25%Fe	25%Fe
25 GPa	0.634	4.485	0.694	3.322	0.738	2.719
75 GPa	0.446	0.809	0.524	0.844	0.583	0.868
125 GPa	0.372	0.882	0.434	0.759	0.471	0.633
	K _{D2} (x=0.5)					
	2000 K		2500 K		3000 K	
	6.25%Fe	25%Fe	6.25%Fe	25%Fe	6.25%Fe	25%Fe
25 GPa	0.407	0.227	0.487	0.305	0.549	0.372
75 GPa	0.190	0.006	0.264	0.016	0.330	0.031
125 GPa	0.070	0.002	0.114	0.005	0.155	0.010

575
576
577
578
579
580
581
582 **Table 2:** Value of ΔS_{vib}-Fe (the change in the vibrational entropy term from replacing a Mg atom with an Fe
 583 atom) for adding 1 iron to 80-atom bridgmanite (Fe%=6.25) and the mixed phase with Ca%=50.

ΔS _{vib} -Fe (meV/atom)			
Pressure (GPa)	Temperature (K)	Bridgmanite	Mixed Phase
25	1000	-2.6	-0.3
	2000	-2.2	-0.1
	3000	-1.6	-0.3
125	1000	-4.1	-4.0
	2000	-4.0	-3.9
	3000	-3.8	-4.4

585
586
587

Figure 1

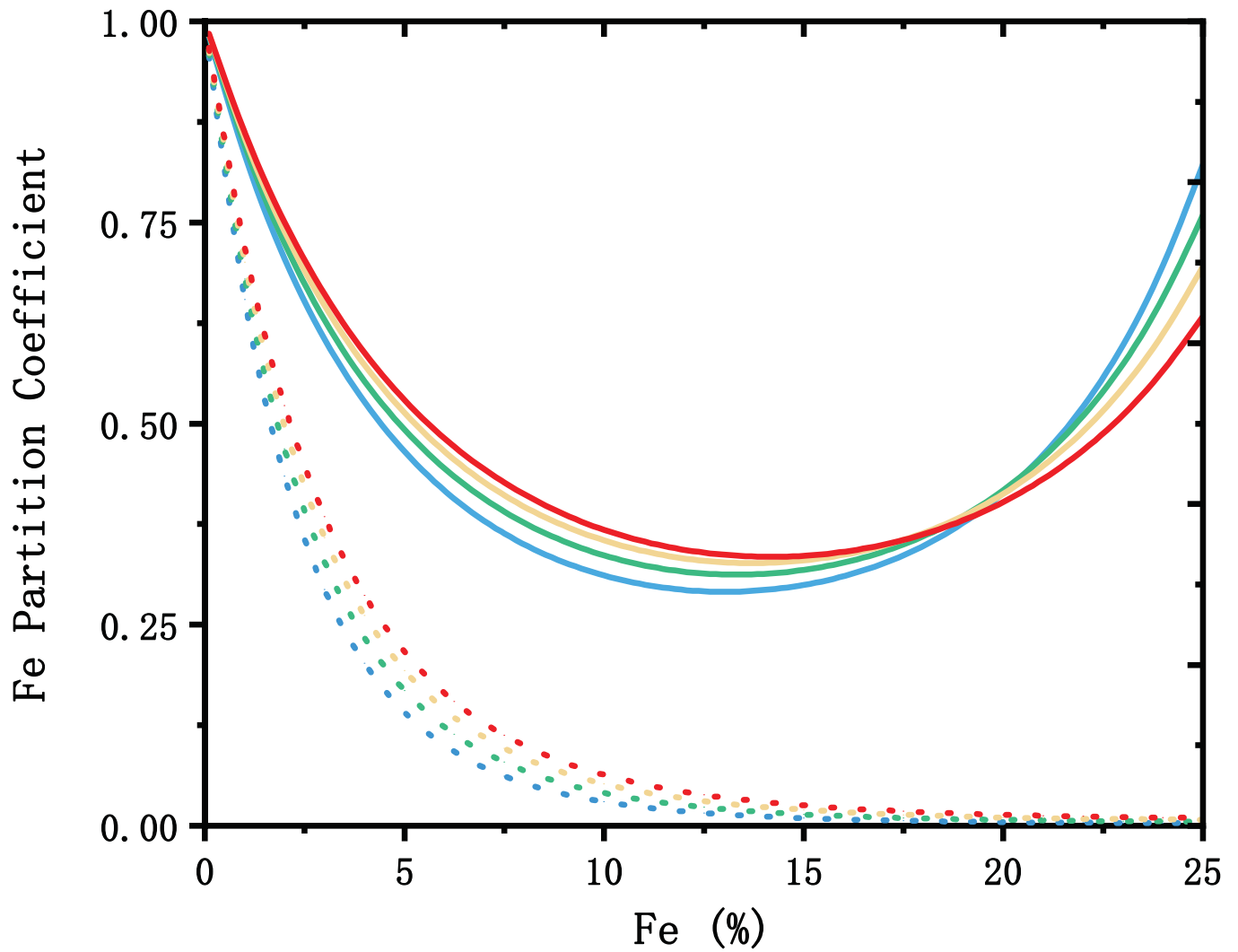


Figure 2

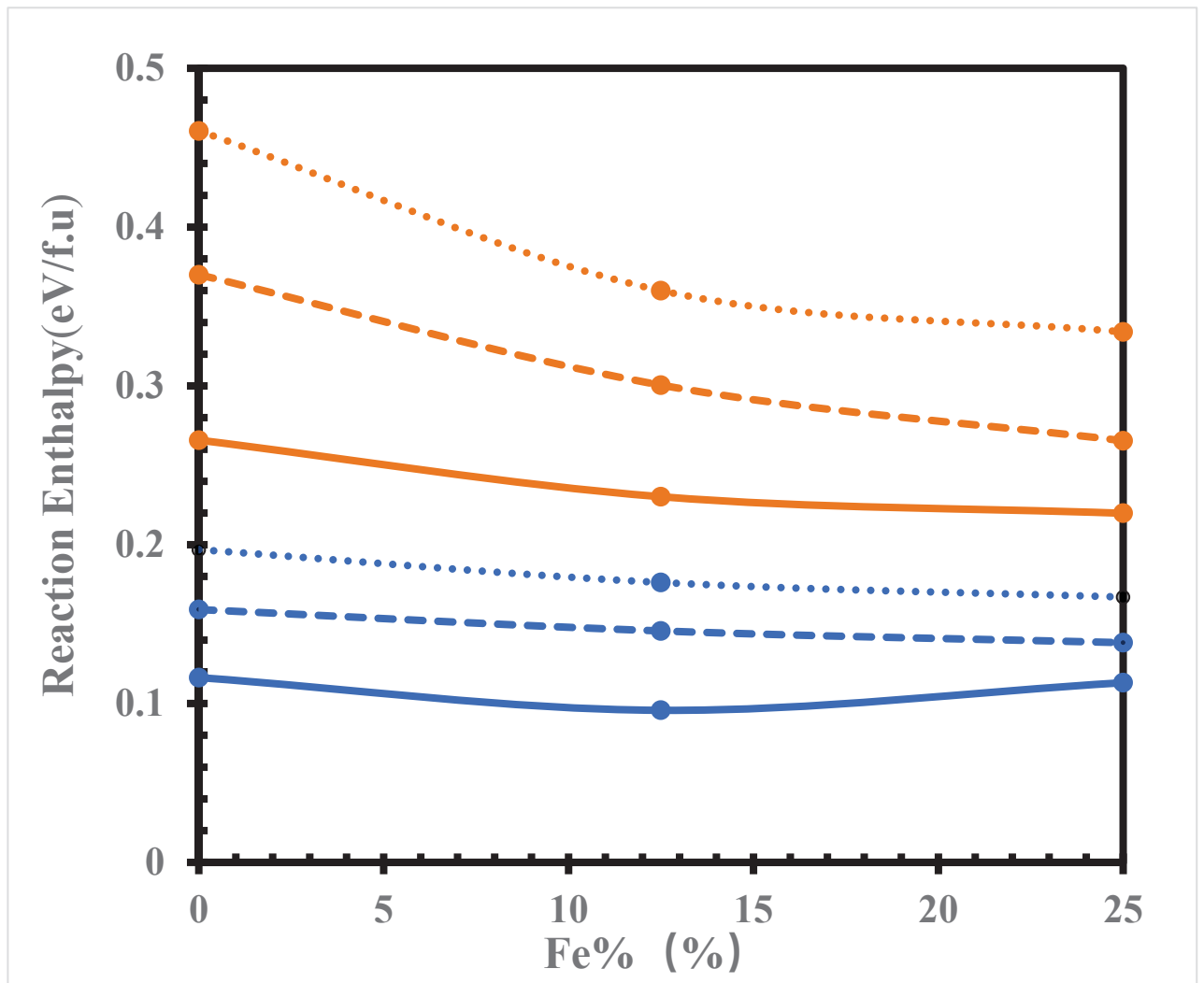


Figure 3

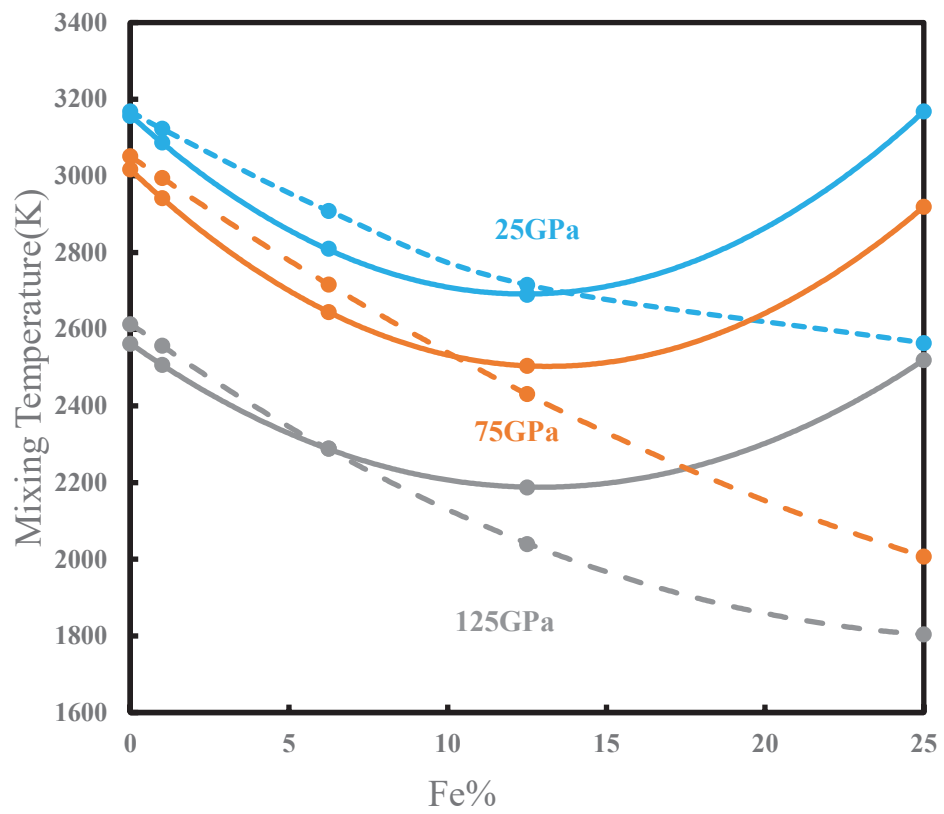


Figure 4

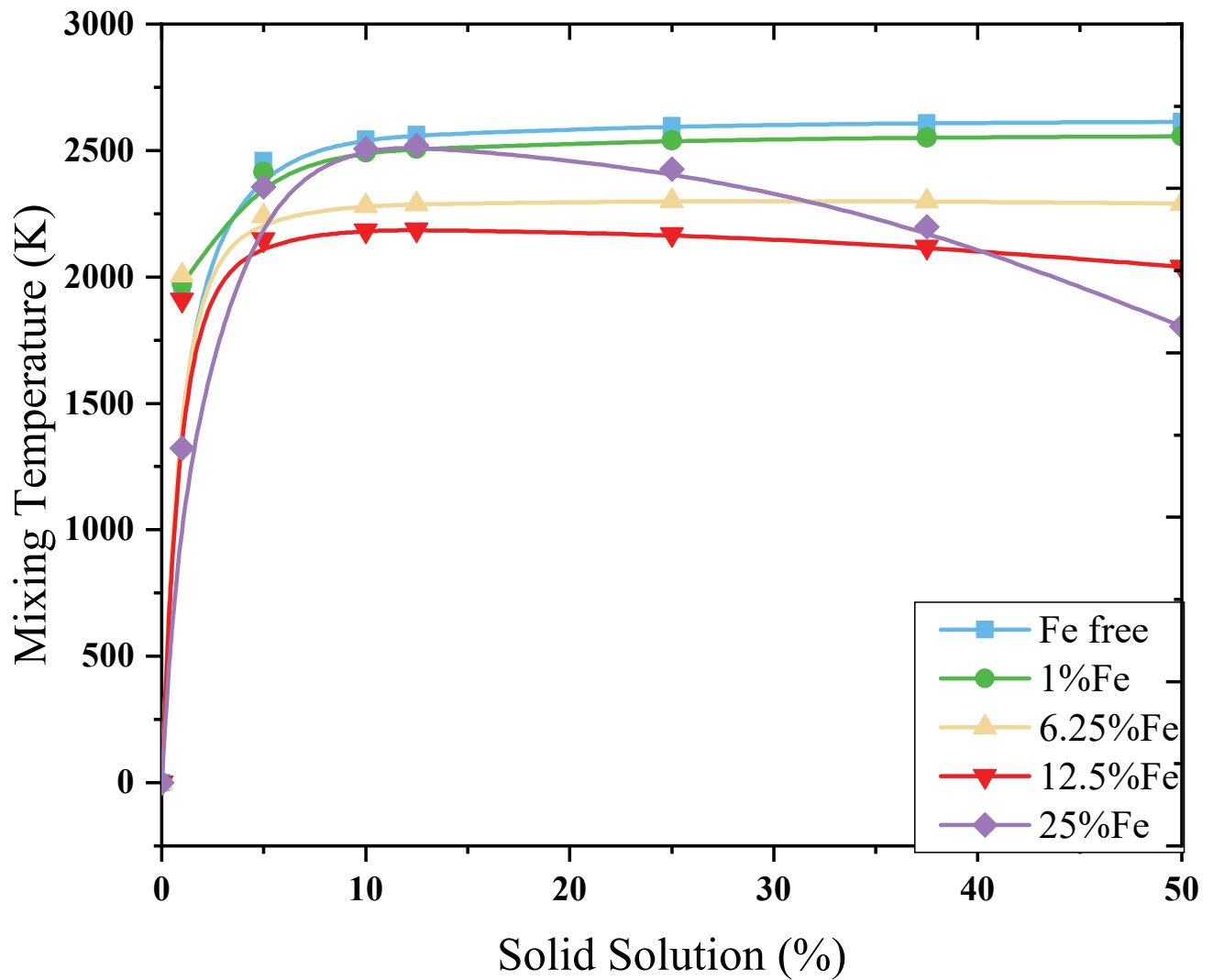


Figure 5

